bioRxiv preprint doi: https://doi.org/10.1101/2024.02.26.582030; this version posted February 28, 2024. The copyright holder for this preprint (which was not certified by peer review) is the author/funder, who has granted bioRxiv a license to display the preprint in perpetuity. It is made available under aCC-BY-NC-ND 4.0 International license.

A quantitative model for *in vivo* stem cell decisions in planarians

Tamar Frankovits[1], Prakash Varkey Cherian[1], Yarden Yasherim[1], Simon Dobler[1,2], Omri Wurtzel[1,3]

[1] The School of Neurobiology, Biochemistry & Biophysics, George S. Wise Faculty of Life Sciences, Tel Aviv University, Tel Aviv, Israel

[2] Present address: Interfaculty Institute of Microbiology and Infection Medicine, University of Tübingen, Tübingen, Germany

[3] Sagol School of Neuroscience, Tel Aviv University, Tel Aviv, Israel

* Correspondence: owurtzel@tauex.tau.ac.il

Abstract

Stem cells contribute to organismal homeostasis by balancing division, self-renewal and differentiation. Elucidating the strategies by which stem cells achieve this balance is critical for understanding homeostasis, and for addressing pathogenesis associated with the disruption of this balance (e.g., cancer). Mathematical models have been developed to distill the principles underlying adult stem cell dynamics in vertebrates. Yet, valuable insights can be derived from modeling invertebrate stem cell systems that rely on a fundamentally different strategy. Here, integrating experimental, computational, and analytical approaches, we develop a quantitative model that reveals basic principles of clonal growth of individual neoblasts – pluripotent planarian stem cells. Deriving key physiological parameter values from experimental data, we show that neoblast colony growth can be well described as a straightforward stochastic decision process, without assuming memory or communication among cells. Crucially, by experimentally suppressing differentiation to major lineages, we reveal the interplay between colony growth and lineage decisions. Our findings suggest that neoblasts pre-select their progenitor lineage based on an underlying cell fate distribution, and that arresting differentiation into specific lineages disrupts neoblasts' proliferative capacity – without inducing compensatory expression of other lineages. Our findings uncover essential aspects of stem cell regulation in planarians, demonstrating how principles distinct from those of vertebrate models can lead to robust homeostatic mechanisms.

bioRxiv preprint doi: https://doi.org/10.1101/2024.02.26.582030; this version posted February 28, 2024. The copyright holder for this preprint (which was not certified by peer review) is the author/funder, who has granted bioRxiv a license to display the preprint in perpetuity. It is made available under aCC-BY-NC-ND 4.0 International license.

Introduction

Stem cells are crucial for achieving and maintaining homeostasis. Paradoxically, they contribute to an organism's equilibrium through highly dynamic behavior, continuously balancing their population size by regulating division, self-renewal, and differentiation. Understanding the strategies used to accomplish this balance can provide the key to elucidating organismal homeostasis, as well as to modeling pathogenesis associated with disruption to this balance (e.g., cancer) [1,2].

Mathematical models provide a means of distilling the complex biological dynamics that make up stem cell behavior into a set of basic underlying principles, which can potentially be used to predict the system's response to various perturbations. Indeed, numerous mathematical and computational models have been developed to describe the dynamics of adult stem cells in vertebrates [3,4]. Yet, valuable insights can be derived from modeling stem cell systems that rely on principles that differ significantly from those characterizing vertebrate stem cells. Neoblasts – adult planarian stem cells that function in tissue regeneration and maintenance – provide an intriguing platform in this regard. Neoblasts are pluripotent, avoid quiescence, and quickly adapt to changes in organismal requirements by adjusting the quantities and types of cells they produce [5]. Significantly, neoblast strategies to grow and maintain planarian tissues challenge fundamental concepts of vertebrate stem cells. For example, in adult vertebrates, hematopoietic stem cells typically divide slowly, giving rise to rapidly dividing transit amplifying cells forming tissue-specific progenitors [6,7]; these, in turn, bear the primary responsibility for maintaining homeostasis. Planarian neoblasts, in contrast, divide rapidly and do not employ transit amplifying cells for progeny production [8–10]. Moreover, neoblasts do not seem to retain memory of the progeny cell types they generate [8,9]. Notably, despite being essentially ageless and immortal, neoblasts do not display cancerous-like states [11]. Therefore, elucidating how neoblasts balance division, self-renewal, and differentiation can contribute to understanding fundamental strategies that facilitate tissue homeostasis [12].

Prior models of neoblast dynamics in planarians have tended to focus on the entire animal system [13]. However, analyzing isolated neoblasts and their progeny can be instrumental for understanding how decisions are made at a single cell resolution, as well as for deriving physiological parameter values (e.g., corresponding to proliferation and differentiation) that are relevant to the larger system. *In vivo* analysis of individual neoblasts and their progeny is often achieved by applying subtotal irradiation to whole

bioRxiv preprint doi: https://doi.org/10.1101/2024.02.26.582030; this version posted February 28, 2024. The copyright holder for this preprint (which was not certified by peer review) is the author/funder, who has granted bioRxiv a license to display the preprint in perpetuity. It is made available under aCC-BY-NC-ND 4.0 International license.

planarians, which results in near-complete neoblast ablation [5]. Surviving neoblasts proliferate to form distinct colonies, allowing analysis of growth dynamics and progeny identity [14,15]. Though such analysis has been instrumental in uncovering regulators of proliferation and differentiation [14], a mathematical model of neoblast colony growth that integrates these principles has yet to be established and experimentally validated.

Several open questions must be taken into account in the development of such a model. For example, it is unclear whether neoblasts select their lineage identity in a synchronous manner or function independently [16,17]. Moreover, as indicated above, it is unclear whether neoblasts maintain memory of their decisions over successive rounds of cell cycles [10]. In addition, as discussed in what follows, critical knowledge is lacking regarding the ability of neoblasts to switch from producing differentiating lineage to contributing to neoblast colony growth; an understanding of this switch is fundamental to accurately capturing the overall development of a neoblast colony.

Herein, we begin to address these gaps, integrating experimental, analytical, and simulation approaches to develop a minimal model for neoblast colony growth. Our model does not assume communication between neoblasts or memory of cell fate decisions; rather, it explores whether straightforward stochastic selection of division outcome can adequately describe the growth of a neoblast colony. At the basis of our model is the assumption, based on *in vivo* analysis of neoblast clone growth, that neoblast division can result in three potential outcomes (Fig. 1) [8,15]: (1) symmetric renewal, which generates two neoblasts; (2) symmetric differentiation, which generates two post-mitotic cells; and (3) asymmetric division, which produces a neoblast and a post-mitotic cell.

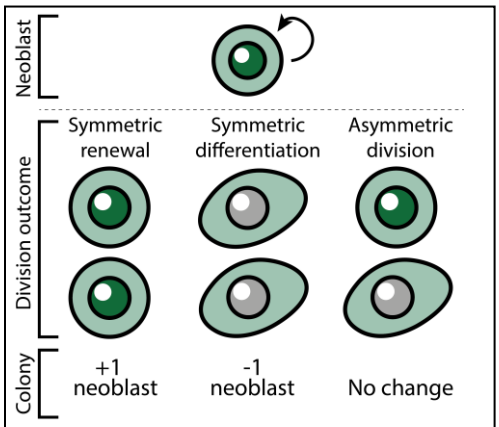

Figure 1. Potential outcomes of neoblast division and the effect on colony size

In what follows, we first put forward a basic model of colony growth based on these principles. We derive key parameter values from experimental data and show that our model predicts colony growth with high accuracy. Next, in a series of experiments, we seek to uncover whether the core principles that drive neoblast colony growth (as proposed in our model) are further shaped by individual neoblasts' decisions regarding progeny lineage commitment. In particular, many S/G2/M neoblasts express fate-specifying

bioRxiv preprint doi: https://doi.org/10.1101/2024.02.26.582030; this version posted February 28, 2024. The copyright holder for this preprint (which was not certified by peer review) is the author/funder, who has granted bioRxiv a license to display the preprint in perpetuity. It is made available under aCC-BY-NC-ND 4.0 International license.

transcription factors (FSTFs), which direct the differentiation of their progeny into specific lineages [18–20]. Importantly, a neoblast can express different FSTFs in successive rounds of division, which results in production of post-mitotic progenitors of different lineages [8,9]. Thus, the growth potential of the colony is not compromised by FSTF expression. Yet, it remains unclear how the growth of a colony might be affected when expression of a particular FSTF (and thus the corresponding cell lineage) is blocked: for example, does colony growth remain stable, with other lineages being overexpressed to compensate for the blocked lineage? Notably, our experimental perturbation analysis shows that blocking the expression of an FSTF incapacitates a proportion of neoblasts equivalent to the size of the lineage affected. This observation reveals a critical dependency: once a neoblast commits to a specific lineage, it retains this identity until cell division concludes.

Together, our findings imply that simple design principles govern cell fate choices in neoblasts, and that accurate prediction of colony growth does not require assumptions of fate-specification memory, or coordination of cell fate choices between neoblasts. Moreover, our findings suggest that all neoblasts in a colony are functionally equivalent (i.e., able to self renew and to divide to all cell types), and elucidate the contribution of decisions in individual planarian stem cells to achieving systemic homeostasis.

Results

Basic model for neoblast colony growth

We developed a minimal model describing neoblast colony growth starting from a single neoblast, simulating a scenario where a surviving neoblast post-subtotal irradiation proliferates to form a colony. This colony serves as the exclusive source of new cells [5,14]. To estimate the change in colony size over time, we formulated an equation representing the exponential growth of a colony successfully established by a surviving neoblast (Eq. 1). In addition to the initial colony size (N_0), the function incorporates three parameters to estimate colony growth (Eq. 2): (1) average cell cycle length (τ); (2) symmetric renewal probability (p), where symmetric renewal rate per hour is $p' = p\tau$; and (3) symmetric differentiation or neoblast elimination probability (q), where symmetric differentiation or neoblast elimination rate per hour is $q' = q\tau$. Asymmetric divisions do not alter neoblast count (Fig 1).

$$\frac{dN}{dt} = p'N - q'N = (p\tau - q\tau)N \qquad [1]$$

bioRxiv preprint doi: https://doi.org/10.1101/2024.02.26.582030; this version posted February 28, 2024. The copyright holder for this preprint (which was not certified by peer review) is the author/funder, who has granted bioRxiv a license to display the preprint in perpetuity. It is made available under aCC-BY-NC-ND 4.0 International license.

We used the solution to the equation to predict colony sizes using a range of parameter values and evaluated the model predictions (Fig 2A; Fig S1) using our own and published data [8,14].

$$N(t) = N_0 e^{(p\tau - q\tau)t} \quad [2]$$

The plots in Fig. 2A show how varying the value of each growth parameter is predicted to affect colony size. The rate of cell division (τ) has the most substantial impact on colony growth. For example, a simulated colony with a fast (16 hours) cell cycle (with p and q set at 0.5 and 0.1, respectively) had a neoblast count approximately ten times larger than that reported in literature [5,8,14,15,20]. To determine the average cell cycle rate (τ), we re-analyzed available colony growth data that had previously been obtained in experiments using Bromodeoxyuridine (BrdU) metabolic labeling [15]. In those experiments, BrdU was incorporated into DNA during both symmetric and asymmetric divisions using a pulse significantly shorter than the cell cycle (4 hours), followed by a chase of up to 72 hours (Fig 2B). We predicted that the $BrdU^+$ cell number would grow linearly until the entire population doubles. Then, completion of successive cell divisions would lead to exponential growth in $BrdU^+$ cell number. Indeed, the colony growth was initially linear (Pearson r = 0.997), and using linear regression, we estimated that the colony doubling time, and hence the average cell cycle length, was 29.7 hours (Fig 2B).

The symmetric renewal probability (p) is also a vital factor in colony growth, where even slight variations in p have large cumulative effects (Fig 2A). We experimentally determined the symmetric renewal probability by subjecting planarians to subtotal irradiation (1750 rad; Methods) and identifying neoblasts via fluorescence *in situ* hybridization (FISH) with the *smedwi-1* marker [21]. We imaged adjacent *smedwi-1*$^+$ cell pairs in the colony, and classified *smedwi-1*$^+$ cell pairs based on their *smedwi-1* expression levels: high-level pairs indicated symmetric renewal, while pairs with one high and one low *smedwi-1*$^+$ cell categorized as asymmetric division. Analysis of 40 dividing pairs produced an estimated symmetric renewal probability (p) of 50% (Fig 2C), aligning with previous findings [8,15].

The value of q, representing symmetric differentiation and neoblast loss probability, also plays a role in colony dynamics (Fig 2B, S1B). Yet the value of this parameter is more difficult to estimate experimentally (e.g., naïve measurement of cell death using TUNEL in irradiated planarians would be insufficient, because cell death is not limited to neoblasts). Using simulations, we analyzed the effect of different neoblast elimination probabilities on colony size (Fig 2D; Fig S1B-E), and compared the model estimates with colony

bioRxiv preprint doi: https://doi.org/10.1101/2024.02.26.582030; this version posted February 28, 2024. The copyright holder for this preprint (which was not certified by peer review) is the author/funder, who has granted bioRxiv a license to display the preprint in perpetuity. It is made available under aCC-BY-NC-ND 4.0 International license.

size in our experimental data and by extracting colony size measurements from published literature (Fig 2D-E;) [5,8,14] (Methods). Considering *p* of 0.5 and an average cell cycle length of 29.7 hours, the experimental data indicated that the average colony size was affected by symmetric differentiation or death probability (*q*), estimated at ~15% of the neoblasts in each cycle (Fig 2D, Fig S1B-E). Given the values derived for *p* and *q*, we can conclude that asymmetrically dividing neoblasts account for 35% of cell divisions (Fig 2F).

In vivo, we observed a large variation in the size of the colonies at each time point (Fig 2E). This could be a consequence of altered delay between irradiation and the onset of colony growth, or from a stochastic decision to undergo symmetrical or asymmetrical division in the early colony. Despite this variability, the observed exponential growth suggested a steady proliferation rate once the colony founding neoblast recovered at day four (Fig 2D, S1A).

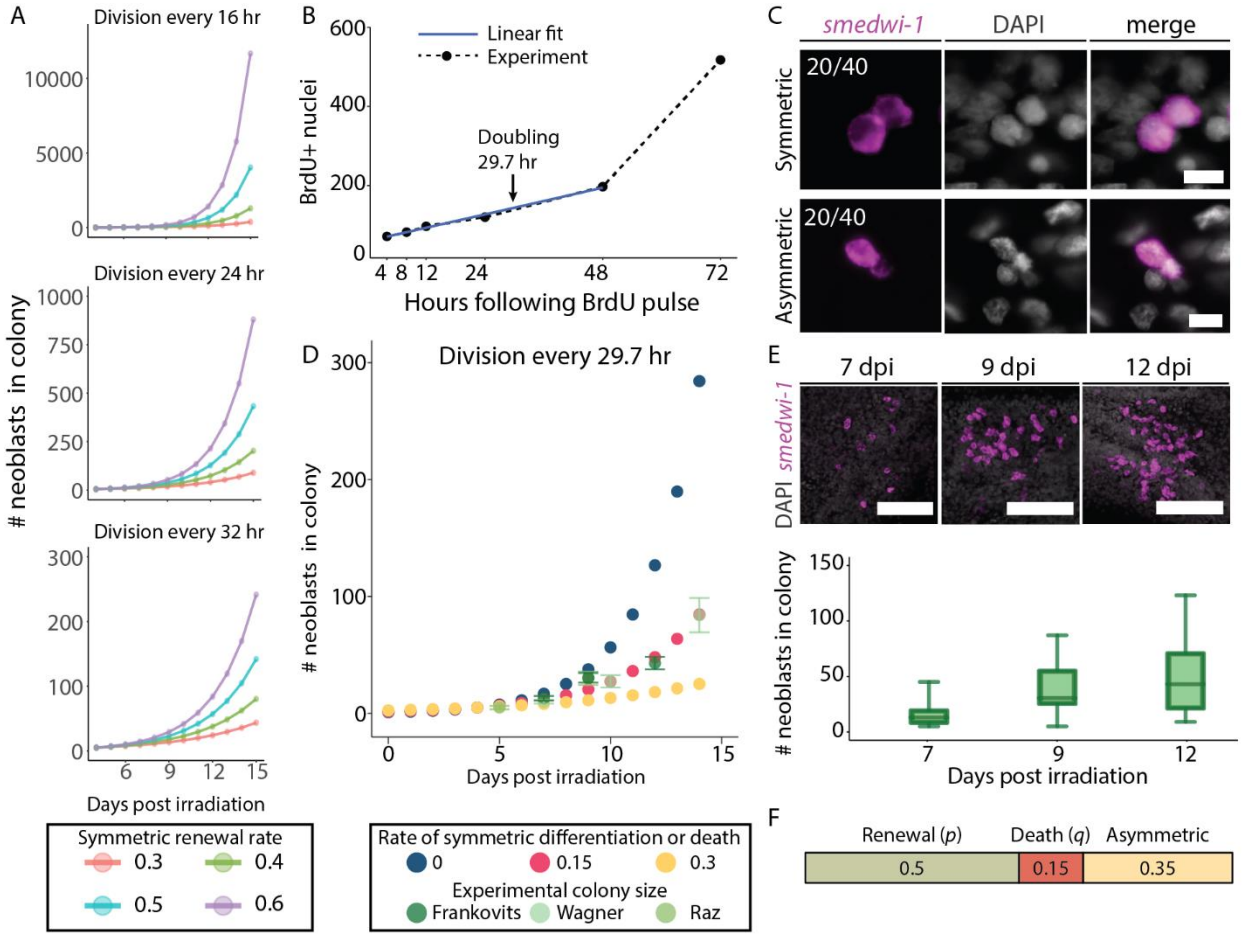

bioRxiv preprint doi: https://doi.org/10.1101/2024.02.26.582030; this version posted February 28, 2024. The copyright holder for this preprint (which was not certified by peer review) is the author/funder, who has granted bioRxiv a license to display the preprint in perpetuity. It is made available under aCC-BY-NC-ND 4.0 International license.

Figure 2. Parameters determining neoblast colony size. (A) The impact of average cell cycle duration and fraction of symmetric renewal division on colony size is shown. (B) Re-analysis of BrdU incorporation time series [15] **in expanding planarian colonies was used for determining the average cell cycle length (Methods). Linear regression (blue line; y = 59.77 + 2.81 * t; Pearson r = 0.997) was used to identify the doubling time of the colony, and was determined as 29.7 hours (black arrow). (C) The fraction of symmetric renewal divisions was estimated by examining neoblast pairs in colonies (Methods). Scale = 10 µm. (D) The impact of symmetric differentiation or neoblast elimination on colony size was tested, assuming a 29.7 hour long cell cycle and 50% symmetric renewal divisions. Experimental data of colony sizes at different time points were overlaid to determine the biologically-relevant parameter. Frankovits data collected here; Wagner, reanalysis** [14]**; Raz, reanalysis** [8]**. Error bars show the standard error. (E) Shown are neoblast colonies at three time points following subtotal irradiation. Representative images (z- projection) are shown (top), and neoblast counting of different colonies is shown (box indicates interquartile range; whiskers show range; horizontal bar indicates median). Scale = 100 µm. (F) The estimated fractions of divisions leading to symmetric renewal, symmetric differentiation or elimination, and asymmetric divisions.**

Inhibition of lineage differentiation reduces neoblast colony size

Regulating growth and homeostasis requires balancing self-renewal and progeny production. To better understand how neoblasts maintain this balance, we focused on the interplay between the overall growth of the colony and the ability of individual neoblasts to express FSTFs, which are required for specific progeny production [19]. More specifically, we investigated how inhibiting differentiation into specific lineages, by suppressing FSTF expression, influences colony size. Considering the linear correlation between post-mitotic progeny production and neoblast number [9,14], we hypothesized three potential outcomes (Fig 3A) and their probable effects on symmetric renewal (*p*) and symmetric differentiation or elimination (*q*): (1) Unchanged: *p* and *q* remain balanced, resulting in no change in colony size. This outcome would suggest that the balance of self-renewal and progeny generation is preserved through compensatory production of alternative cell types when differentiation to a specific lineage is suppressed. (2) Larger: An increase in *p*, leading to larger colonies, possibly due to fewer asymmetric divisions in the blocked lineage. (3) Smaller: An increase in *q*, leading to smaller colonies, possibly because neoblasts committed to the blocked lineage become dysfunctional. We used published frequencies of three major lineages (epidermis, intestine, and *foxF-1*$^{+}$ neoblasts) to estimate the size of the colony in each of the described scenarios (Fig 3A) [9,19,22]. Theoretically, inhibiting a predominant lineage, such as the epidermal lineage (28%), may significantly affect colony size, which could be observed experimentally, whereas changes in colony size following inhibition of smaller lineages could be difficult to distinguish in the experiment time scale.

bioRxiv preprint doi: https://doi.org/10.1101/2024.02.26.582030; this version posted February 28, 2024. The copyright holder for this preprint (which was not certified by peer review) is the author/funder, who has granted bioRxiv a license to display the preprint in perpetuity. It is made available under aCC-BY-NC-ND 4.0 International license.

On the basis of this assumption, we inhibited differentiation into the epidermal lineage after subtotally irradiating planarians. Following a four-day recovery after subtotal irradiation, we suppressed the FSTF *zfp-1*, which is critical for production of differentiating epidermal progenitors (Fig S2) [5,9,23,24]. Then, we evaluated neoblast colony sizes in *zfp-1*-suppressed (*zfp-1* (RNAi)) planarians at three time points (7, 9, and 12 days post-irradiation; dpi), and compared them with control colony sizes (Fig 3B, Methods). Initially (7 dpi), colony sizes were similar. However, at 9 dpi, *zfp-1* (RNAi) colonies were significantly smaller than in controls. Moreover, unlike in controls, *zfp-1* (RNAi) colonies showed no additional growth, on average, during the period between 9 dpi and 12 dpi, though there was a slight increase in the median colony size (Fig 3B).

Our basic assumption was that reduction in colony size (vs. control) following *zfp-1* inhibition would indicate an increase in symmetric differentiation or elimination (*q*). However, an alternative possibility is that *zfp-1* inhibition causes mitotic arrest in neoblasts—which would prevent proliferation but would not necessarily result in cell death. We tested whether *zfp-1* (RNAi) colonies had a lower number of cycling neoblasts. We detected neoblasts in mitosis using immunofluorescence (IF) with an anti-H3P-antibody (Fig 3C; Methods). We found that control colonies did not significantly differ from *zfp-1* (RNAi) colonies in the number of $H3P^+$ cells, either in absolute numbers or normalized to average neoblast counts (Methods). This result suggested that FSTF inhibition did not cause a general mitotic arrest. Further analysis with 2'-Deoxy-2'-fluoro-5-ethynyluridine (EdU) labeling (Fig 3D; Methods) showed a substantial decrease in EdU^+ nuclei in *zfp-1* (RNAi) animals (vs. controls), indicating reduced new cell production. However, normalizing EdU^+ nuclei to average colony size (Fig 3D; Methods) revealed a comparable proportion of cells entering S-phase. Given the unchanged ratios of cycling and mitotic cells, we can conclude that the diminished colony size following *zfp-1* suppression is indeed likely to result either from increased symmetric differentiation or neoblast elimination (*q*). We further suggest that neoblast elimination is a more plausible explanation than increased symmetric differentiation: If *zfp-1* suppression were to lead to increased symmetric differentiation, we would expect to observe a noticeable decline in the number of neoblasts within colonies, while proliferation rates remained stable. Yet, our EdU-labeling experiments suggested a reduction in proliferation rates, suggesting that inhibition of the FSTF *zfp-1* likely led to increased neoblast elimination.

bioRxiv preprint doi: https://doi.org/10.1101/2024.02.26.582030; this version posted February 28, 2024. The copyright holder for this preprint (which was not certified by peer review) is the author/funder, who has granted bioRxiv a license to display the preprint in perpetuity. It is made available under aCC-BY-NC-ND 4.0 International license.

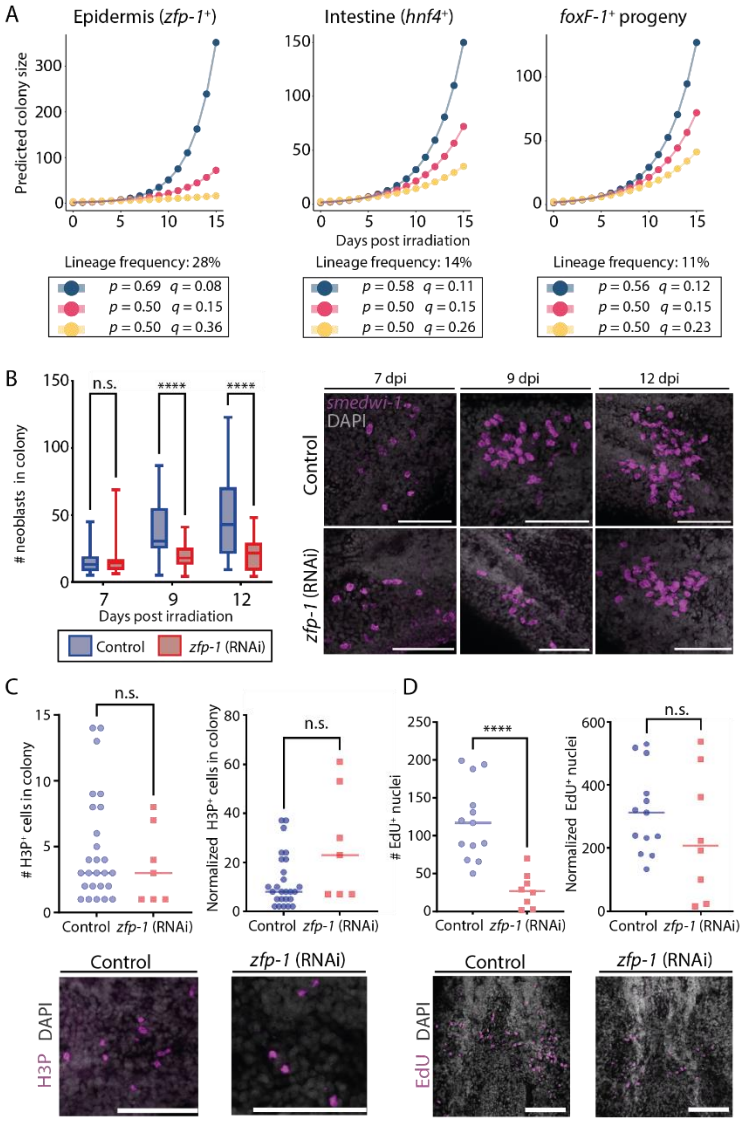

Figure 3. Reduced neoblast colony size following lineage specification block. (A) Models for lineage growth. Potential outcomes of lineage inhibitions were assessed by altering the colony growth and degradation parameters. Applying known lineage frequencies to the models indicated that inhibiting production of a major lineage could dramatically impact colony size (left, epidermis). By contrast, inhibition of smaller lineages (middle, right) might have a smaller impact, which would be difficult to detect (Blue: increase in symmetric renewal; red: unchanged renewal and degradation; yellow: increase neoblast degradation). (B) Shown are counts (left) of neoblasts in colonies at three time points following irradiation, which was followed by inhibition of *zfp-1* by RNAi. Lineage inhibition resulted in a highly significant decrease in colony size at later time points (box indicates interquartile range (IQR), whiskers show range, bar indicates the median). Number of control colonies analyzed at 7 dpi n = 28; at 9 dpi n = 30; at 12 dpi n = 30; Number of *zfp-1* (RNAi) colonies analyzed at 7 dpi n=15; at 9 dpi n=30; at 12 dpi n = 30. Representative colonies (z-projection) are shown (right). (C) Comparison of absolute (top-left) or normalized (top-right) H3P$^+$ cell number in *zfp-1* (RNAi) and control colonies showed a non-significant difference (Methods). Representative H3P labeling images are shown (Bottom). Importantly, the number of detectable H3P+ cells was small. (D) Comparison of (top-left) EdU+

bioRxiv preprint doi: https://doi.org/10.1101/2024.02.26.582030; this version posted February 28, 2024. The copyright holder for this preprint (which was not certified by peer review) is the author/funder, who has granted bioRxiv a license to display the preprint in perpetuity. It is made available under aCC-BY-NC-ND 4.0 International license.

nuclei in *zfp-1* (RNAi) and control colonies showed a significant reduction, contributing to the smaller colony size. Comparison of normalized EdU+ nuclei numbers (top-right) showed a non-significant difference, indicating that a similar proportion of the neoblast in the colony were cycling (Methods). Representative EdU labeling images (z-projection) are shown (Bottom). Statistical significance was assessed using Mann Whitney two-tailed test (Methods). n.s., not significant, *P* <0.05. Scale = 100 µm.

Specialized neoblasts are produced in *zfp-1* (RNAi) colonies

Building upon our findings regarding lineage-specific inhibition effects, we next investigated how RNAi of *zfp-1* affected the prevalence of other specialized neoblasts in colonies. We hypothesized that if neoblast elimination was the primary effect of *zfp-1* inhibition, we would observe an absolute decrease in specialized neoblasts of other lineages (e.g., intestine), but not necessarily a relative decrease. We used subtotal irradiation, and following recovery we inhibited *zfp-1*. Then, we counted specialized neoblasts expressing intestine lineage markers [5,19] , and *tgs-1* [20], which is suggested to label neural progenitors (Fig 4A-B; Methods). Both control and *zfp-1* (RNAi) colonies contained specialized neoblasts. Notably, a decrease in intestine specialized neoblasts was detectable, aligned with the reduced colony size (Fig 4A). Small numbers of *tgs-1*$^{+}$ neoblasts were observed, with no significant reduction in their numbers (Fig 4B). Together, these results suggest that specialized neoblasts were produced in *zfp-1* (RNAi) colonies, but that production of other (non-suppressed) lineages did not increase, suggesting that neoblast elimination predominantly accounts for the reduction in colony size following suppression of the epidermal lineage, without compensation by overproduction of other lineages.

To further analyze the impact of *zfp-1* inhibition on colony growth, we examined the numbers of neoblasts in 64 control colonies and in 53 *zfp-1* (RNAi) colonies, at 12 dpi (Fig 4C-D). The proportion of colonies containing five or more neoblasts was greater in the control group (75%) than in the *zfp-1* (RNAi) group (45%; Fisher's exact test two-tailed $P = 0.001$). Importantly, more *zfp-1* (RNAi) animals failed to develop colonies compared to controls (55% and 25%, *zfp-1* (RNAi) and control colonies, respectively). This might have resulted from the stochastic selection of a *zfp-1* identity by the neoblasts that initially established the colony, and which led to their further dysfunction, and was therefore detrimental to the development of the colony.

bioRxiv preprint doi: https://doi.org/10.1101/2024.02.26.582030; this version posted February 28, 2024. The copyright holder for this preprint (which was not certified by peer review) is the author/funder, who has granted bioRxiv a license to display the preprint in perpetuity. It is made available under aCC-BY-NC-ND 4.0 International license.

Modeling colony growth following *zfp-1* inhibition

We developed a simulation to recapitulate the observed reduction in colony growth following *zfp*-1 inhibition. Our simulation methodology was designed to mimic real-world neoblast dynamics under *zfp-1* inhibition, using empirically derived probabilities for each cell cycle outcome. First, we randomly sampled initial colony sizes from the set counted at 7 dpi (Fig 3B). In every simulation cycle, each neoblast fate was selected based on the probabilities of cell cycle outcomes identified above, derived from empirical data (symmetric renewal, asymmetric division, symmetric differentiation or elimination; Fig 2F). The change in colony size was calculated over approximately six cell cycles. We conducted 100 iterations per simulation and compared the results with experimental data (Fig 4E). The simulated colony sizes closely matched the experimental observations. When simulating *zfp-1* (RNAi) colony growth by increasing the symmetric differentiation or elimination probability (q) by the known proportion of *zfp-1*$^+$ neoblasts, the model accurately replicated the experimental findings (Fig 4E-F). Notably, many simulated *zfp-1* (RNAi) colonies failed to grow, often because of initial sampling of a state of symmetric differentiation or elimination, prohibiting further development of the colony (Fig 4F).

The agreement of these simulations with the experimental results is aligned with a model where neoblasts independently select their cell cycle outcome based on a replication outcome distribution without maintaining any memory of previous replication outcomes. Moreover, inhibition of a gene required for neoblast differentiation (e.g., FSTF) impedes the contribution of neoblasts that randomly selected this identity from any further contribution to colony growth across the timescale of the simulation.

Combined suppression of low-frequency lineages affects neoblast colony formation

Our model and simulations indicate that inhibition of smaller lineages will not result in detectably smaller colonies (Fig S3A-C). We tested this model prediction by comparing colonies produced following suppression of intestine lineage progenitors [5,9,25], which account for 14% of the produced progenitors [8]. Indeed, highly efficient inhibition of the intestine lineage by RNAi (Fig S3D), did not result in reduced colony size or colony production, in agreement with our model (Fig 4G-H, S3A). This result corroborated the model's predictions regarding lower-frequency lineages (Fig 3A): the potential increase in q following suppression of differentiation to a lower-frequency lineage had undetectable effect on colony size. However, the model predicts that inhibition of several lineages, which collectively amount to a larger fraction of produced progenitors, may generate a detectable difference in successful colony

bioRxiv preprint doi: https://doi.org/10.1101/2024.02.26.582030; this version posted February 28, 2024. The copyright holder for this preprint (which was not certified by peer review) is the author/funder, who has granted bioRxiv a license to display the preprint in perpetuity. It is made available under aCC-BY-NC-ND 4.0 International license.

establishment. We co-suppressed the production of intestine lineage together with *foxF-1*$^{+}$ progenitors, which together amount to 25% of the progenitors [8], following subtotal irradiation (Fig 4I). The co-inhibition of the two lineages resulted in a highly significant increase in the failure to establish colonies (8/9; 88.9%), compared to their controls (3/19; 15.8%; Fisher's exact test two-tailed P = 4x10^{-4}).

These results reinforce the hypothesis that FSTF inhibition reduces colony growth (vs. control), primarily through increased neoblast elimination, without compensatory increases in other lineages. The results also suggest that a neoblast that has selected an identity, but that cannot complete proliferation and differentiation, will not be able to adopt any other identity in this experimental timescale. Based on these conclusions, we propose a semi-stochastic model for selecting the outcome of neoblast division, assuming no memory or coordination between cells, that is sufficient for describing the neoblast colony growth.

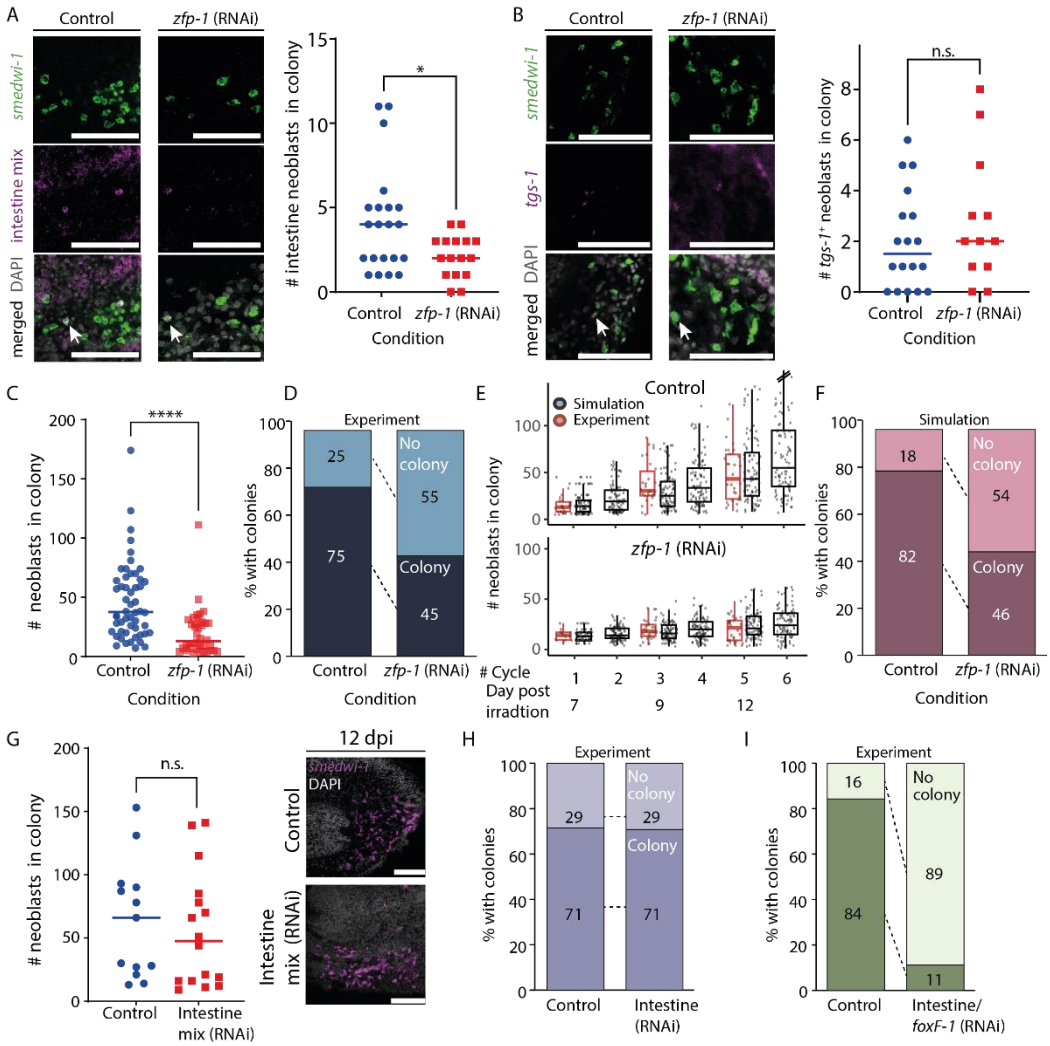

bioRxiv preprint doi: https://doi.org/10.1101/2024.02.26.582030; this version posted February 28, 2024. The copyright holder for this preprint (which was not certified by peer review) is the author/funder, who has granted bioRxiv a license to display the preprint in perpetuity. It is made available under aCC-BY-NC-ND 4.0 International license.

Figure 4. Simulation of neoblast colony growth following lineage block. (A-B) Neoblasts expressing lineage gene expression markers were detected using fluorescence in situ hybridization (intestine mix: *hnf-4, gata4/5/6, nkx2.2*) and hybridization chain reaction (*tgs-1*), and counted in colonies of control and *zfp-1* (RNAi) animals at 12 dpi (Methods). Left panels show confocal images of representative colonies (Methods); quantification of the experiment is shown on the right. Scale= 100 µm. (C) Comparison of colony size in control and in *zfp-1* (RNAi) animals 12 dpi showed a highly significant reduction in the size of *zfp-1* (RNAi) colonies (Mann Whitney two-tailed test, *P* <0.0001). (D) Summary of colony production in control and *zfp-1* (RNAi) animals based on analysis of 64 and 53 control and *zfp-1* (RNAi) colonies, respectively, at 12 dpi. Developed: ≥ 5 neoblasts detected; No colony < 5 neoblasts detected. (E) Simulation of colony growth in control and *zfp-1* (RNAi) animals, bottom and top, respectively (Methods). Shown are multiple iterations (black dots; n = 100 for each condition) of colony size simulation starting at 7 dpi. Experimental data quantifying colony sizes are shown (red dots) next to the corresponding simulation cycle. Box indicates the IQR; whiskers indicate ±1.5 x IQR; values out of the whisker (outliers) were removed for clarity. (F) Summary of colony production in simulated control and *zfp-1* (RNAi) animals based on experimentally determined lineage frequencies, and assuming no memory in division outcome decision. Developed colony: ≥ 5 neoblasts in the simulation at day 12. (G) Neoblasts were counted in colonies 12 days following subtotal irradiation, which was followed by inhibition of intestine progenitors by combined RNAi treatment (*hnf-4*, *gata4/5/6*, *nkx2.2*). Lineage inhibition did not affect colony size (left). Representative colonies (z-projection) are shown (right). Scale = 100 µm. (H-I) Summary of colony establishment in controls and following RNAi. (H) Suppression of intestine lineage did not affect the likelihood of producing colonies (n = 21 and 24, control and RNAi animals, respectively). (I) Combined suppression of *foxF-1* [22] and intestine lineage production resulted in a significant reduction in the likelihood of producing colonies (Fisher's exact test two tailed *P* = $4x10^{-4}$; n = 19 and 9, control and RNAi animals, respectively).

Inhibition of *zfp-1* does not induce overexpression of other lineages in homeostasis

Clonal analysis is a powerful approach for studying neoblast proliferation and progeny production. However, the behavior of stem cells in homeostasis may differ from that observed in clonal growth. For example, unlike in clonal expansion, the stem cell population size remains unchanged during homeostasis (i.e., *p* and *q* are equal). Moreover, the vastness of the neoblast population in homeostasis allows to examine the ability of neoblast to respecify their lineage overtime, and to determine if an FSTF inhibition results in an increase to cell death rate.

We examined whether the suppression of a major lineage production has resulted in overproduction of other lineages, a phenomenon that we did not observe in colonies. First, we used two published gene expression datasets from FACS-purified S/G2/M neoblasts in *zfp-1* (RNAi) and control animals collected at various time points [9,24] (Methods). We utilized a list of differentially expressed genes in these datasets [26], and annotated the cell types that express them [27]. Most downregulated genes with known neoblast lineage enrichment [27] were epidermal (82%, 55/67; Fig 5A; Table S1; Methods). Conversely, upregulated genes following *zfp-1* suppression were primarily associated with protonephridial or neural

bioRxiv preprint doi: https://doi.org/10.1101/2024.02.26.582030; this version posted February 28, 2024. The copyright holder for this preprint (which was not certified by peer review) is the author/funder, who has granted bioRxiv a license to display the preprint in perpetuity. It is made available under aCC-BY-NC-ND 4.0 International license.

neoblasts (30/57 and 20/57 genes, respectively; Fig 5B; Table S2), consistent with the original data analysis [24]. Notable upregulated genes included transcription factors, such as *nkx2-like* [28], *hunchback-like* [29], *runt-1* [30,31], and *tgs-1* [20]. Overexpression was evident from an intermediate timepoint (9 days post RNAi), whereas epidermal genes downregulation occurred earlier (6 days post RNAi; 30%, 20/67; FDR < 1E-5).

We hypothesized that biologically meaningful upregulation of neuron- and protonephridia-associated genes in neoblasts following *zfp-1* inhibition would result in overexpression of genes associated with these cell types in whole tissues, reflecting their increased production. To test this hypothesis, we examined published gene expression data from whole and regenerated tissues in *zfp-1* inhibition [9,20]. Predictably, the majority of downregulated genes were associated with the epidermis (70%, 490/698; Fold change < -2; FDR < 1E-5; Table S3; Methods). Examination of upregulated genes showed that only a small fraction of the genes was associated with either protonephridial (4.9%) or neural (12.7%) expression at any examined time point (Fig 5C; Table S4; Methods). Therefore, gene expression analysis of whole tissues provided no evidence of an overrepresentation of neural or protonephridia cells in *zfp-1* (RNAi) animals, suggesting that cells related to these lineages were not excessively produced. Conversely, 37% of the overexpressed genes following *zfp-1* (RNAi) in the whole tissue libraries were associated with intestinal cell types, despite no evidence for overrepresentation of intestine-associated FSTFs in neoblasts isolated from *zfp-1* (RNAi) animals compared to controls (Table S4).

In *zfp-1* (RNAi) neoblast colonies, we observed an absolute reduction in cycling cells (Fig 3D). We tested whether this phenotype was recapitulated in homeostatic, unirradiated, *zfp-1* (RNAi) animals by EdU labeling. We injected *zfp-1* or control double-stranded (dsRNA) (Methods), and following three and five days, we performed EdU labeling by a 16 hour EdU pulse (Methods). Interestingly, there was an increase in EdU^+ nuclei in the *zfp-1* (RNAi) animals at both timepoints (Fig 5D). Investigating the potential correlation with apoptosis via TUNEL labeling revealed no early increase in cell death, only appearing at later stages (Fig 5E; Methods). Therefore, *zfp-1* inhibition does not trigger an acute rise in neoblast cell death that might induce hyperproliferation.

bioRxiv preprint doi: https://doi.org/10.1101/2024.02.26.582030; this version posted February 28, 2024. The copyright holder for this preprint (which was not certified by peer review) is the author/funder, who has granted bioRxiv a license to display the preprint in perpetuity. It is made available under aCC-BY-NC-ND 4.0 International license.

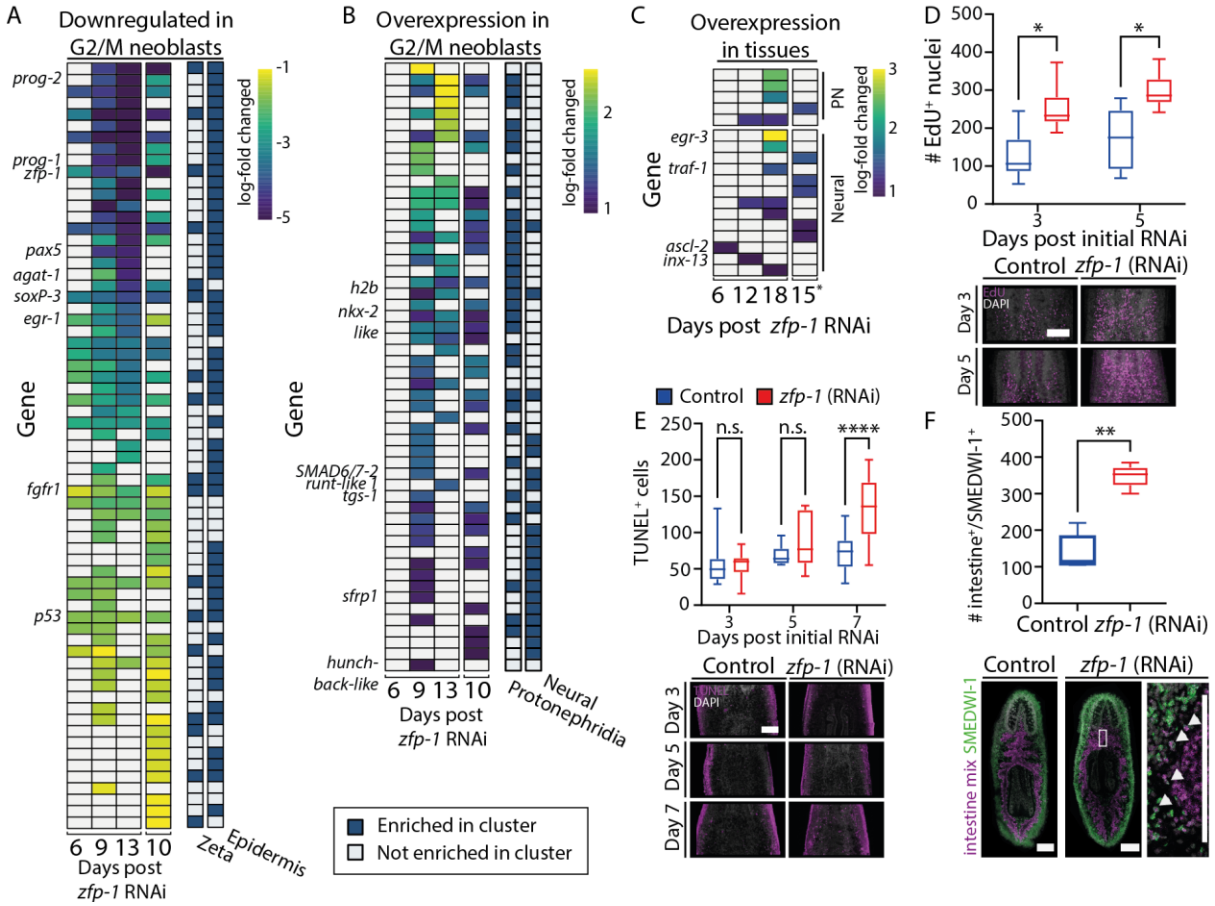

Figure 5. Analysis of *zfp-1* inhibition consequences in homeostasis. (A) Downregulated genes in FACS-purified S/G2/M neoblasts were overwhelmingly associated with expression in the epidermal lineage and epidermal-specialized (zeta) neoblasts [9,24,27] **. (B) Upregulated genes in FACS-purified S/G2/M neoblasts were largely associated with neuronal and protonephridial specialized gene expression** [27]**. (C) Analysis of overexpressed genes of whole-tissues following *zfp-1* inhibition showed that only a few factors were associated with protonephridia or neurons. (A-C) Heatmaps showing row-scaled gene expression obtained from PLANAtools** [26] **Blue and yellow, low and high log-fold gene expression difference, respectively. Columns on the right indicate cell type-specific gene expression** [27]**. (D) Counting EdU+ nuclei in unirradiated control and *zfp-1* (RNAi) animals. (E) Counting apoptotic cells in unirradiated control and *zfp-1* (RNAi) animals (Methods). (F) Counting intestinal progenitors showed an increase in progenitors at later time points, in agreement with the gene expression analysis of *zfp-1* (RNAi) of whole tissues. Scale = 100 µm. *P* < 0.05.**

Colony sizes following *zfp-1* (RNAi) were reduced, yet cycling cell numbers in homeostasis were increased. Similar results were reported for the epidermal regulator *Smed-p53* [24,32]: neoblast colonies following *p53* (RNAi) are strikingly smaller, yet in homeostasis, *p53* (RNAi) animals show an increased number of mitoses [32], and even initially an increase in canonical neoblast markers [32].

bioRxiv preprint doi: https://doi.org/10.1101/2024.02.26.582030; this version posted February 28, 2024. The copyright holder for this preprint (which was not certified by peer review) is the author/funder, who has granted bioRxiv a license to display the preprint in perpetuity. It is made available under aCC-BY-NC-ND 4.0 International license.

Considering that in homeostasis *zfp-1* (RNAi) planarians show greater numbers of cycling cells (Fig 5D) and intestinal gene overexpression in tissue (Table S4) as compared with controls, we conducted a targeted analysis to quantify the number of newly generated intestine progenitors in *zfp-1* (RNAi) animals. We counted intestine progenitors *in situ* (Fig 5F; Methods), and found a higher proportion of intestine progenitors in the *zfp-1* (RNAi) animals as compared with controls (Fig 5F; Mann–Whitney two-tailed U test $P = 0.008$). Interestingly, in our analyses of growing colonies, we did not observe a parallel difference in intestine neoblast proportion (Fig 4A), leading us to speculate that the rise in cycling cells in homeostasis was an indirect effect of *zfp-1* (RNAi). In other words, integration of the analysis from homeostasis with our colony data suggests that *zfp-1* inhibition did not lead to a direct amplification of other lineages, but more likely to an indirect amplification of the intestine lineage.

Discussion

Understanding how stem cell proliferation and lineage choices are regulated is critical for elucidating mechanisms of growth and homeostasis [15,33–39]. Neoblasts form a simple yet powerful system, which has features of both adult stem cells and their transit-amplifying cell progeny [16,40,41]. Functionally, neoblasts can repopulate stem cell-depleted planarians, produce a diversity of cell types, and adjust their growth rate according to organism requirement and nutrient availability [42–45]. Herein, we sought to test whether a simple model (Fig 6) that does not assume communication between neoblasts or memory of cell fate decisions, and instead uses stochastic selection of division outcome, can predict the growth of a neoblast colony. We further sought to enrich this model with an understanding of the interplay between neoblast lineage decisions and colony growth – which has been missing from the literature thus far.

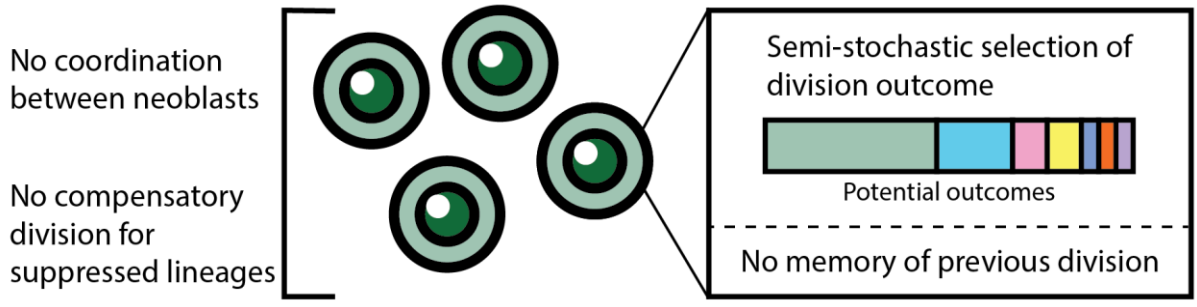

Figure 6. Model summarizing neoblast colony growth principles.

bioRxiv preprint doi: https://doi.org/10.1101/2024.02.26.582030; this version posted February 28, 2024. The copyright holder for this preprint (which was not certified by peer review) is the author/funder, who has granted bioRxiv a license to display the preprint in perpetuity. It is made available under aCC-BY-NC-ND 4.0 International license.

Predictive modeling of neoblast colony expansion

The initial model we developed was grounded in simple principles of colony growth (Equation 1, Fig. 2A), in which cell fate decisions are made stochastically and independently of one another, as a function of the following parameters: average cell cycle length, symmetric renewal rate, and symmetric differentiation and neoblast elimination rate. We experimentally derived parameter values and compared the model's predictions to experimental data. Our findings suggested that the reliance on minimal assumptions provides a good description of neoblast colony growth following subtotal irradiation. The model captured the average colony growth within the tested time range despite notable variability in observed colony sizes at a given time point. Based on these results, we suggest that if slow cycling neoblasts emerge in colonies, their contribution for colony growth is likely negligible, allowing their exclusion from the model without sacrificing accuracy.

To better understand the potential consequences of random cell death or excessive symmetric differentiation at early stages of colony growth, we used colony growth simulations, where each cell selected independently the outcome of its division. These simulations predicted that a fraction of colonies would fail to develop because of these random effects, a prediction that was corroborated by experimental results. This alignment demonstrates the utility of neoblasts as a system for studying stem cell colony formation and exploring concepts of stem cell behavior.

Consequences of lineage-specific differentiation inhibition

Moving from the fundamental aspects of neoblast colony growth, we next tested how limiting lineage identity selection affected neoblasts. We suppressed the expression of key fate-specifying genes to dissect how stem cells respond to inhibition of their differentiation trajectory. The transition from modeling general colony growth to specific lineage perturbations enabled us to examine the association of proliferation and lineage specification. In particular, suppressing the master epidermal regulator *zfp-1*, corresponding to the most abundant planarian cell lineage [8,9,24], drastically reduced neoblast colony growth rate. This observation led us to consider how stem cells balance self-renewal and differentiation, and why both processes were disrupted by blocking differentiation to a single lineage. We suggest several interpretations for this observation: First, if we assume that a neoblast can alternate between self-renewal and production of differentiated progeny in each cell cycle, then a decision to produce a blocked progeny may preclude further divisions of the neoblast. A second possibility is that the presence of specific

bioRxiv preprint doi: https://doi.org/10.1101/2024.02.26.582030; this version posted February 28, 2024. The copyright holder for this preprint (which was not certified by peer review) is the author/funder, who has granted bioRxiv a license to display the preprint in perpetuity. It is made available under aCC-BY-NC-ND 4.0 International license.

lineage, epidermal progenitors in this case, is required for other neoblasts to proliferate; in this case, suppression of differentiation could indirectly limit colony growth. The first interpretation is more likely relevant for understanding colony growth given our observation that combined suppression of several smaller lineages produced a similar inhibition to colony establishment.

The progressive reduction in colony size indicated that inhibition of a specific lineage reduced the fraction of neoblasts that contributed to colony growth, possibly due to their failure to produce the blocked lineage and to alter their progeny identity. Interestingly, in unirradiated animals with abundant neoblasts, *zfp-1* inhibition led to increased cell proliferation – a response also noted after suppressing other regulatory genes like *Smed-p53* [32]. This proliferation increase appeared before a rise in cell death, suggesting that cell death did not induce excessive proliferation in early stages. The difference in the consequence of lineage suppression in a neoblast colony and in unirradiated animals indicates that further investigation is needed into compensatory mechanisms that planarians use to maintain overall tissue integrity when differentiation processes are disrupted.

A stochastic model for independent selection of cell division outcome in colonies

Our study investigates the mechanism behind neoblast division outcome selection. An exponential growth model accurately predicts the increase in colony size and the differentiation of progeny, closely aligning with experimental results [8,14]. Notably, our model operates without parameters for coordination of division outcome between neoblasts, or neoblast memory. It posits that division outcomes are determined by a stochastic process [46], guided by an innate distribution of cell fates encoded within the neoblasts. We hypothesize that this distribution is modifiable by regional signals (e.g., Wnt, BMP), which indicate the neoblast location [47–49], and by injury signals (e.g., ERK), that modulate division rate [17,50–52]. This strategy facilitates the dynamic balance in cell lineage production and meeting the organism needs without direct communication between neoblasts, and promotes return to homeostasis.

The emerging model enhances the understanding of neoblast dynamics and contributes to broader knowledge of stem cell behavior. The interplay between lineage-specific differentiation, proliferation, and resultant physiological adaptations presents a robust strategy for using pluripotent stem cells for re-achieving balance, in a manner that is not found in many non-regenerative organisms. This could inspire future research of pluripotent stem cells and their applications for regenerative biology.

bioRxiv preprint doi: https://doi.org/10.1101/2024.02.26.582030; this version posted February 28, 2024. The copyright holder for this preprint (which was not certified by peer review) is the author/funder, who has granted bioRxiv a license to display the preprint in perpetuity. It is made available under aCC-BY-NC-ND 4.0 International license.

Methods

Gene cloning and transformation

Selected genes were amplified using planarian cDNA and gene-specific primers, and cloned into pGEM-T Easy vector using pGEM-T Easy Vector System I (Promega; CAT A1360). Vectors were transformed into *Escherichia coli* using the heat-shock method. Briefly, 5 µl of cloned plasmid were mixed with 100 µl of *E. coli* TOP10 bacteria and incubated on ice for 30 min. Next, bacteria were incubated for 45 s at 42°C, moved immediately to ice, and recovered in 350 µl of Luria Broth (LB) medium for 1 h at 37°C. Then, 100 µl of recovered bacteria were plated on agarose plates containing 1:1,000 Ampicillin, 1:200 Isopropyl β- d-1-thiogalactopyranoside (IPTG) and 1:625 5-bromo-4-chloro-3-indolyl-b-D-galactopyranoside (X-Gal). Plates were incubated overnight at 37°C, and colonies were screened by colony PCR using M13F and M13R primers with the following PCR program: (i) 5 min at 95°C; (ii) 34 cycles of 45 s at 95°C, 60 s at 55°C, and 2 min at 72°C; (iii) 7 min at 72°C; (iv) hold at 10°C. Reactions were analyzed by gel electrophoresis, and colonies having the correct fragment were grown overnight in LB medium, supplemented with 1:1,000 Ampicillin at 37°C in 180 rpm. Plasmids were purified with the NucleoSpin Plasmid MiniprepKit (CAT 740588, Macherey-Nagel) and sequenced by Sanger sequencing. Primer sequences used for cloning the following genes: *hnf-4*, forward primer GATCTCGCACAATGCACTCG, reverse primer GTCTCACGAACTCCTTGCCA; *nkx2.2*, forward primer TTTGGTGCCAGCAGACTCAA, reverse primer TAGAGCCAGCTAATGTGGCG; *gata4/5/6*, forward primer CGGTATTGTCGAATTCTCACCAG, reverse primer TGACATCGCAATTGGAACCG; *foxF-1*, forward primer GTCCTATTTCCAGCACACAGC, reverse primer TCCGGAATCGTGCTGAGG.

Near complete neoblast ablation by subtotal irradiation

Animals were irradiated using a BIOBEAM GM 8000 (Gamma-Service Medical GmbH). To generate 1-3 colonies per animal, 2 mm starved (> 7 d) worms were irradiated with 1750 rads [14]. Worms were allowed to recover and washed in planarian water a day after the irradiation.

Synthesis of dsRNA for feedings and microinjections

DsRNA was synthesized as previously described [53]. Briefly, templates for in vitro transcription (IVT) were prepared by PCR amplification of cloned target genes using forward and reverse primers with flanking T7 promoter sequences on the 5’ end. dsRNA was synthesized using the TranscriptAid T7 High Yield Transcription Kit (CAT K0441, Thermo Scientific). Reactions were incubated overnight at 37°C and then

bioRxiv preprint doi: https://doi.org/10.1101/2024.02.26.582030; this version posted February 28, 2024. The copyright holder for this preprint (which was not certified by peer review) is the author/funder, who has granted bioRxiv a license to display the preprint in perpetuity. It is made available under aCC-BY-NC-ND 4.0 International license.

supplemented with RNase-free DNase for 30 min. RNA was purified by ethanol precipitation and resuspended in 70 µl of ultra-pure H2O. RNA was analyzed on 1% agarose gel and quantified by Qubit (CAT Q33223, Thermo Scientific) for validating a concentration higher than 5 µg/µl. Animals were starved for at least 7 d prior to RNAi experiments. In clonal expansion experiments, animals were fed with 14 µl of dsRNA mixed with 25 µl of beef liver 4 days post-irradiation. In homeostasis experiments, worms were injected 4 times with dsRNA every other day.

Injections of dsRNA into planarians

Animals were injected with *zfp-1* dsRNA using Nanoject III (CAT 3-000-207, Drummond Scientific company). Briefly, planarians were placed on a cold wet filter paper on their dorsal side, and were injected posterior to the pharyngeal cavity. After the initial puncture, 3 consecutive dsRNA injections of 33 nl each were delivered at a rate of 66 nl/sec. Worms were injected 4 times, every other day, and fixed at different time points for whole-mount analysis.

Planarian fixation for whole-mount assays

Fixation was performed as previously described [54]. Animals were killed with 5% N-Acetyl-L-Cysteine (NAC, CAT 1124220100, Mercury) in PBS for 5 min, then incubated with 4% Formaldehyde (FA) in 0.3% PBSTx (Phosphate Buffered Saline, 0.3% Triton X-100) for 20 min. Animals were then washed in PBSTx, 50:50 PBSTx:methanol and stored in methanol at -20°C.

Fluorescence in situ hybridization using tyramide signal amplification

Fluorescence in situ hybridization (FISH) was performed as previously described [54] with minor changes. Briefly, fixed animals were bleached and treated with proteinase K (2 µg/ml, CAT 25530-049; Invitrogen) in PBSTx (Phosphate Buffered Saline, 0.3% Triton X-100). Samples were incubated for 2 hr in a pre-hybridization buffer (pre-hyb) followed by an overnight incubation with probes. Samples were washed twice for 30 min in each solution: pre-hyb solution, 1:1 pre-hyb:2×SSCx, 2×SSCx, 0.2×SSCx, PBSTx. Blocking was performed in 0.5% Roche Western Blocking Reagent (CAT 11921673001; Sigma-Aldrich) and 5% heat-inactivated horse serum (CAT 04-124-1A; Biological Industries) in TNTx (100 mM Tris pH 7.5, 150 mM NaCl, 0.3% Triton X-100) for 2 hr. Animals were incubated with an anti-DIG-POD antibody (1:1,500; Roche) or anti-DNP-HRP (1:10,000; Perkin-Elmer) overnight at 4°C. After antibody washes, tyramide development was performed as previously described [55]. Following development, peroxidase activation was quenched in a 1% sodium azide solution for 1 hr, followed by 6 PBSTx washes and antibody labeling for the second

bioRxiv preprint doi: https://doi.org/10.1101/2024.02.26.582030; this version posted February 28, 2024. The copyright holder for this preprint (which was not certified by peer review) is the author/funder, who has granted bioRxiv a license to display the preprint in perpetuity. It is made available under aCC-BY-NC-ND 4.0 International license.

528 probe. Samples were labeled with DAPI (1:5000 in PBSTx) overnight at 4°C and mounted with Vectasheild
529 (CAT H-1000-10; Vector Laboratories).

530 **Immunofluorescence combined with FISH**

531 Animals were fixed with 5% NAC, bleached, and treated with proteinase K as described for FISH analysis.
532 Samples were incubated for 2 hr in pre-hyb followed by overnight incubation with the probes. Samples
533 were washed twice in each solution, for 30 min each: pre-hyb solution, 1:1 pre-hyb:2×SSCx, 2×SSCx,
534 0.2×SSCx, PBSTx. Subsequently, blocking was performed in PBSTB (PBSTx, 0.25% BSA) for 2 hr at room
535 temperature. Animals were then incubated with anti-SMEDWI-1 antibody (a gift from Peter W. Reddien,
536 1:1000) at 4°C overnight. Then, 7 PBSTx washes were performed, followed by incubation with PBSTB
537 blocking solution for 2 hr at room temperature followed by incubation with secondary antibody (goat anti
538 rabbit-HRP, 1:300 in PBSTB) overnight at 4°C. Post-antibody washes and tyramide development
539 (fluorescein tyramide; 1:2000) were performed as previously described [54]. After development,
540 peroxidase activity was quenched using 1% sodium azide for 1 hr, followed by 6 PBSTx washes and
541 incubation with anti-DIG antibody (1:1,500; CAT 11207733910; Sigma-Aldrich) overnight at 4°C. Post-
542 antibody washes and development with rhodamine tyramide (1:1000) were performed as described
543 above. Samples were incubated with DAPI (1:5000 in PBSTx) overnight and mounted with Vectashield.
544

545 **FISH by hybridization chain reaction**

546 Probe sets (30 pairs per gene) were designed and synthesized by the manufacturer (Molecular
547 Instruments, Los Angeles, CA, USA) for the following genes: *tgs-1* and *smedwi-1*. Worms were fixed and
548 bleached as previously described for FISH. Next, hybridization chain reaction (HCR) was performed
549 according to the manufacturer's HCR RNA-FISH protocol for samples in solution [56]. DAPI was added
550 during the amplifier's wash steps, for a total incubation time of 2 hr at room temperature. Samples were
551 mounted with Vectashield and stored at 4°C for subsequent analysis.

552 **Metabolic labeling by F-ara-EdU**

553 F-ara-EdU (CAT T511293; Sigma-Aldrich) was first diluted in DMSO to the concentration of 200 mg/ml.
554 Animals were soaked with 2.5 mg/ml F-ara-EdU diluted in planarian water for 16 hr, 24 hr after the
555 indicated injections. For clonal expansion analysis, samples were soaked with EdU for 16 hr at day 11 post
556 irradiation. Samples were fixed, bleached, and treated with proteinase K as described for FISH [54]. Next,

bioRxiv preprint doi: https://doi.org/10.1101/2024.02.26.582030; this version posted February 28, 2024. The copyright holder for this preprint (which was not certified by peer review) is the author/funder, who has granted bioRxiv a license to display the preprint in perpetuity. It is made available under aCC-BY-NC-ND 4.0 International license.

3 washes in 3% PBSB (PBS supplemented with 3% BSA) were performed followed by a click reaction using baseclick kit (CAT Back-edu488, baseclick GmbH). Samples were washed 3 times with PBSB, incubated with DAPI (1:5,000 in PBSTx) overnight at 4°C and mounted with Vectashield.

Immunofluorescence labeling by anti-H3P labeling

H3P labeling was performed as previously described [46,57] with minor modifications. Briefly, following fixation with 5% NAC, bleaching and proteinase K treatment, blocking was performed with 10% heat inactivated horse serum for 2 hr. Next, anti-phospho-Histone H3 Antibody (CAT 04817; Sigma-Aldrich) was added in the concentration of 1:100 overnight in 4°C, followed by 7 PBSTx washes. Samples were incubated in blocking solution for 2 hr and then incubated with goat anti-rabbit-HRP secondary antibody (Abcam; ab6721; 1:300) overnight at 4°C. Samples were washed 7 times with PBSTx, developed using rhodamine tyramide diluted 1:1,000 in PBSTi (PBSTx, 0.07% imidazole), labeled with DAPI overnight at 4°C, and mounted with Vectashield.

Image acquisition and cell counting

Images of samples labeled by FISH, HCR, immunofluorescence, F-ara-EdU and TUNEL were collected using a Zeiss LSM800 confocal microscope. Labeled cells were counted manually using the cell counter module in the ImageJ software [58].

TUNEL labeling

TUNEL was performed as previously described [59] with minor modifications. Briefly, animals were fixed with 5% NAC and bleached overnight with 6% hydrogen peroxide in PBSTx. Animals were then treated with 2 µg/ml proteinase K for 10 min, 4% FA for 10 min, and were then washed twice with PBS. Using ApopTag Red In Situ Apoptosis Detection Kit (CAT S7165; Sigma-Aldrich), 5 animals per tube were incubated with TdT enzyme mix for 4 hr at 37°C, followed by 4 PBSTx washes. Samples were incubated in a blocking solution (0.5% Roche Western Blocking Reagent and 5% inactivated horse serum in TNTx) for 2 hr followed by incubation with anti-DIG antibody (1:1000) overnight at 4°C. Samples were washed 7 times with PBSTx, developed using rhodamine tyramide diluted 1:1,000, labeled with DAPI (1:5000 in PBSTx) overnight at 4°C and mounted with Vectashield.

bioRxiv preprint doi: https://doi.org/10.1101/2024.02.26.582030; this version posted February 28, 2024. The copyright holder for this preprint (which was not certified by peer review) is the author/funder, who has granted bioRxiv a license to display the preprint in perpetuity. It is made available under aCC-BY-NC-ND 4.0 International license.

Estimation of the fraction of symmetric renewal divisions

Colonies from 7, 9, and 12 dpi were labeled by FISH with the pan-neoblast marker *smedwi-1.* Colonies were closely examined using a confocal microscope (Zeiss LSM800) to find two adjacent *smedwi-1*+ cells. Two labeled cells with high expression of *smedwi-1* marker were classified as symmetric division. Pairs composed of high *smedwi-1*+ cell and low *smedwi-1*+ cell were classified as asymmetrically dividing.

Data extraction from published literature

Data was extracted using WebPlotDigitizer by labeling data points [60]. Table S5 summarizes the extracted data and the original data source.

Simulation of colony growth

Simulations were performed using custom R code, executing as follows: selection of parameters occurred using selected frequencies of symmetric renewal, and symmetric differentiation or elimination. Initial colony size was determined by randomly selecting a value from empirical distribution of early colony size, as reported in the literature [5,8]. In each simulation round, every cell underwent selection of an outcome, adhering to the predefined frequencies. This simulation process extended up to 20 cycles and was replicated 1000 times.

Gene expression analysis of S/G2/M neoblasts

Processed differential gene expression data profiling FACS-purified S/G2/M neoblasts isolated from control and *zfp-1* (RNAi) animals was downloaded from PLANATools [26]. Each gene in the table was assigned a cell type identity based on the planarian cell type gene expression atlas [27].

Statistical analyses

Statistical tests were performed using GraphPad Prism (v 10.0.3) or using the scipy stat module (v 1.12). Statistical significance was assessed using Mann-Whitney two-tailed U test or two-tailed Student's t test and threshold for considering an effect significant was 0.05, unless stated otherwise.

bioRxiv preprint doi: https://doi.org/10.1101/2024.02.26.582030; this version posted February 28, 2024. The copyright holder for this preprint (which was not certified by peer review) is the author/funder, who has granted bioRxiv a license to display the preprint in perpetuity. It is made available under aCC-BY-NC-ND 4.0 International license.

Supplementary Figures

Figure S1

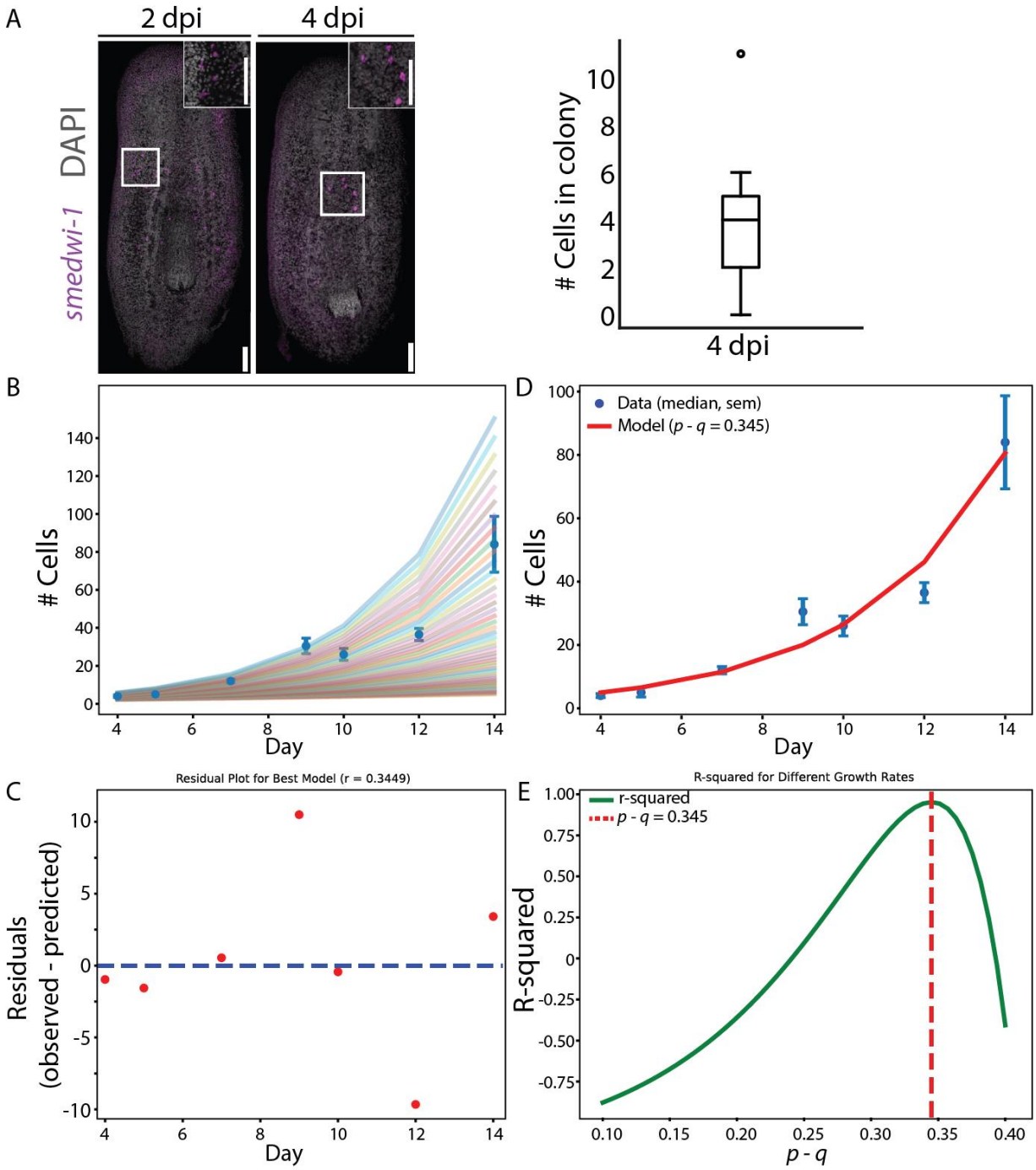

Figure S1. Analysis of colony growth. (A) Shown are FISH images for detecting neoblasts (*smedwi-1*$^+$; magenta) at 2 and 4 days post irradiation (dpi), left and right, respectively. Colonies were not found at 2 dpi, and instead isolated *smedwi-1*+ were scattered in the planarian parenchyma. At 4 dpi, single neoblasts already established small colonies (median = 4 cells;

bioRxiv preprint doi: https://doi.org/10.1101/2024.02.26.582030; this version posted February 28, 2024. The copyright holder for this preprint (which was not certified by peer review) is the author/funder, who has granted bioRxiv a license to display the preprint in perpetuity. It is made available under aCC-BY-NC-ND 4.0 International license.

quantification shown on right). (B-E) The effect of different growth parameters on colony size. (B) Shown are colony sizes when considering a range of *q* values (0.1 - 0.4) with the experimentally determined *p* = 0.5. Data collected here and in published analyses of colony sizes [8,14] **is shown as median (blue dots, and standard error of the mean). (C) Shown is the best predicted fit growth following colony establishment using the exponential growth equation. (D) Analysis of residuals between observed and predicted colony sizes using the best fitting parameters. (E) Shown is the r-squared difference between observed and predicted data at a range of growth parameters. The minimal r-squared value is indicated by the red dashed line.**

Figure S2

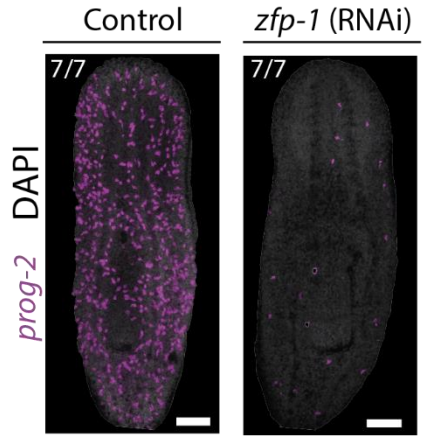

Figure S2. Inhibition of epidermal progenitors by a single *zfp-1* dsRNA injection. Inhibition of *zfp-1* resulted in complete ablation of epidermal progenitor production as observed by labeling animals with the epidermal progenitor marker, *prog-2*.

bioRxiv preprint doi: https://doi.org/10.1101/2024.02.26.582030; this version posted February 28, 2024. The copyright holder for this preprint (which was not certified by peer review) is the author/funder, who has granted bioRxiv a license to display the preprint in perpetuity. It is made available under aCC-BY-NC-ND 4.0 International license.

Figure S3

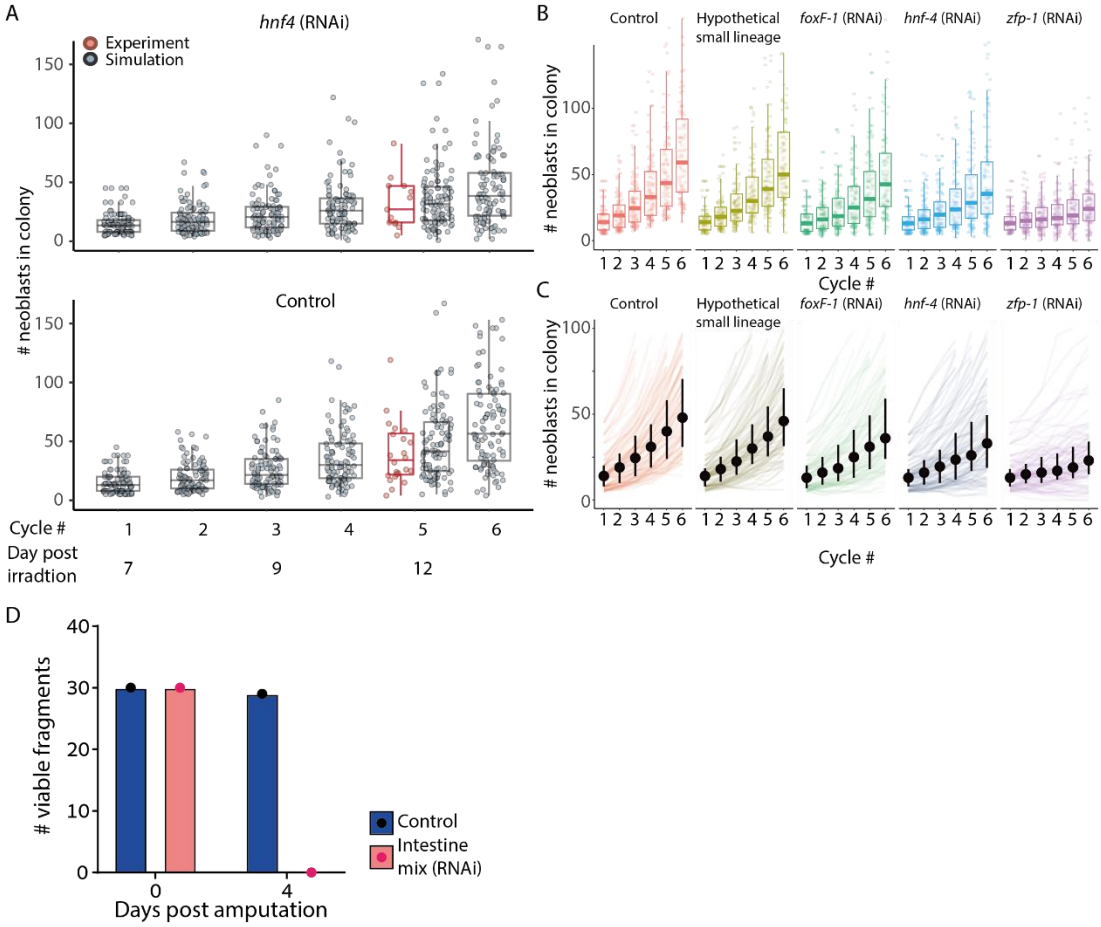

Figure S3. Simulation of colony size following RNAi. (A) Simulation (gray) and comparison to experimental data (red) of neoblast colonies in control and *hnf-4* (RNAi) animals. The simulation indicates that given the variability in colony size, detecting significant differences colony size is unlikely for this lineage. Each dot represents a single simulation (gray) or an experimentally determined size (red). (B-C) Simulations of colony sizes over 6 cycles of replication starting approximately at day seven post irradiation. (B) Boxplots showing the distribution of colony sizes (horizontal line, median; box, interquartile range (IQR); vertical line, 99% range). Each dot represents a single simulation. (C) Simulation of colony growth (line) shows growth over time (dot, median; vertical line, IQR). (D) The RNAi efficacy was evaluated through assessment of viability of fragments obtained from animals following a single feeding of dsRNA that targeted intestine FSTFs (*hnf-4, gata4/5/6, nkx2.2*), compared to a non-targeting control dsRNA (*unc22*). All fragments derived from worms fed with dsRNA targeting intestine FSTFs died within four days post-feeding, demonstrating that a single dsRNA feeding induced a robust effect.

bioRxiv preprint doi: https://doi.org/10.1101/2024.02.26.582030; this version posted February 28, 2024. The copyright holder for this preprint (which was not certified by peer review) is the author/funder, who has granted bioRxiv a license to display the preprint in perpetuity. It is made available under aCC-BY-NC-ND 4.0 International license.

Supplementary Tables

Table S1

Table S1. Downregulated genes in G2/M neoblasts following *zfp-1* (RNAi)

Table S2

Table S2. Upregulated genes in G2/M neoblasts following *zfp-1* (RNAi).

Table S3

Table S3. Downregulated genes in tissues or blastema following *zfp-1* (RNAi)

Table S4

Table S4. Upregulated genes in tissues or blastema following *zfp-1* (RNAi)

Table S5

Table S5. Summary of data extraction using WebPlotDigitizer

Author contributions

T.F. and O.W. designed the project. T.F. performed all experiments with support from P.V.C, Y.Y., and S.D.. T.F. performed microscopy and imaging analysis. O.W. performed simulations and RNAseq data analysis. T.F. and O.W. wrote and edited the manuscript.

Conflict of interest

The authors do not have conflict of interests to declare.

Acknowledgements

We thank Prof. David Sprinzak and Dr. Yasmine Meroz for their critical input. We thank Shrey Jain for his assistance with performing FISH. We thank members of the Wurtzel lab for feedback and discussions. We thank Dr. Daria Makarovsky from the interdepartmental services at Tel Aviv University's Faculty of

bioRxiv preprint doi: https://doi.org/10.1101/2024.02.26.582030; this version posted February 28, 2024. The copyright holder for this preprint (which was not certified by peer review) is the author/funder, who has granted bioRxiv a license to display the preprint in perpetuity. It is made available under aCC-BY-NC-ND 4.0 International license.

659 Medicine for assistance with gamma irradiation. O.W. is supported by the Israel Science Foundation
660 (grant 2039/18) and the European Research Council (no. 853640). O.W. is a Zuckerman Faculty Scholar.
661

bioRxiv preprint doi: https://doi.org/10.1101/2024.02.26.582030; this version posted February 28, 2024. The copyright holder for this preprint (which was not certified by peer review) is the author/funder, who has granted bioRxiv a license to display the preprint in perpetuity. It is made available under aCC-BY-NC-ND 4.0 International license.

References

1. Singh, S.R., Burnicka-Turek, O., Chauhan, C., and Hou, S.X. (2011). Spermatogonial stem cells, infertility and testicular cancer. J. Cell. Mol. Med. *15*, 468–483.

2. Passegué, E., Jamieson, C.H.M., Ailles, L.E., and Weissman, I.L. (2003). Normal and leukemic hematopoiesis: are leukemias a stem cell disorder or a reacquisition of stem cell characteristics? Proc Natl Acad Sci USA *100 Suppl 1*, 11842–11849.

3. Marciniak-Czochra, A., Stiehl, T., Ho, A.D., Jäger, W., and Wagner, W. (2009). Modeling of asymmetric cell division in hematopoietic stem cells--regulation of self-renewal is essential for efficient repopulation. Stem Cells Dev. *18*, 377–385.

4. Paździorek, P.R. (2014). Mathematical model of stem cell differentiation and tissue regeneration with stochastic noise. Bull. Math. Biol. *76*, 1642–1669.

5. Wagner, D.E., Wang, I.E., and Reddien, P.W. (2011). Clonogenic neoblasts are pluripotent adult stem cells that underlie planarian regeneration. Science *332*, 811–816.

6. Abkowitz, J.L., Golinelli, D., Harrison, D.E., and Guttorp, P. (2000). In vivo kinetics of murine hemopoietic stem cells. Blood *96*, 3399–3405.

7. Becker, K.A., Ghule, P.N., Therrien, J.A., Lian, J.B., Stein, J.L., van Wijnen, A.J., and Stein, G.S. (2006). Self-renewal of human embryonic stem cells is supported by a shortened G1 cell cycle phase. J. Cell. Physiol. *209*, 883–893.

8. Raz, A.A., Wurtzel, O., and Reddien, P.W. (2021). Planarian stem cells specify fate yet retain potency during the cell cycle. Cell Stem Cell *28*, 1307-1322.e5.

9. van Wolfswinkel, J.C., Wagner, D.E., and Reddien, P.W. (2014). Single-cell analysis reveals functionally distinct classes within the planarian stem cell compartment. Cell Stem Cell *15*, 326–339.

10. Pearson, B.J. (2022). Finding the potency in planarians. Commun. Biol. *5*, 970.

11. Van Roten, A., Barakat, A.Z.A.-Z., Wouters, A., Tran, T.A., Mouton, S., Noben, J.-P., Gentile, L., and Smeets, K. (2018). A carcinogenic trigger to study the function of tumor suppressor genes in *Schmidtea mediterranea*. Dis. Model. Mech. *11*.

12. Levin, M., Pietak, A.M., and Bischof, J. (2019). Planarian regeneration as a model of anatomical homeostasis: Recent progress in biophysical and computational approaches. Semin. Cell Dev. Biol. *87*, 125–144.

13. Mangel, M., Bonsall, M.B., and Aboobaker, A. (2016). Feedback control in planarian stem cell systems. BMC Syst. Biol. *10*, 17.

14. Wagner, D.E., Ho, J.J., and Reddien, P.W. (2012). Genetic regulators of a pluripotent adult stem cell system in planarians identified by RNAi and clonal analysis. Cell Stem Cell *10*, 299–311.

bioRxiv preprint doi: https://doi.org/10.1101/2024.02.26.582030; this version posted February 28, 2024. The copyright holder for this preprint (which was not certified by peer review) is the author/funder, who has granted bioRxiv a license to display the preprint in perpetuity. It is made available under aCC-BY-NC-ND 4.0 International license.

15. Lei, K., Thi-Kim Vu, H., Mohan, R.D., McKinney, S.A., Seidel, C.W., Alexander, R., Gotting, K., Workman, J.L., and Sánchez Alvarado, A. (2016). Egf signaling directs neoblast repopulation by regulating asymmetric cell division in planarians. Dev. Cell *38*, 413–429.

16. Reddien, P.W. (2018). The cellular and molecular basis for planarian regeneration. Cell *175*, 327–345.

17. Bohr, T.E., Shiroor, D.A., and Adler, C.E. (2021). Planarian stem cells sense the identity of the missing pharynx to launch its targeted regeneration. eLife *10*.

18. Reddien, P.W. (2013). Specialized progenitors and regeneration. Development *140*, 951–957.

19. Scimone, M.L., Kravarik, K.M., Lapan, S.W., and Reddien, P.W. (2014). Neoblast specialization in regeneration of the planarian *Schmidtea mediterranea*. Stem Cell Reports *3*, 339–352.

20. Zeng, A., Li, H., Guo, L., Gao, X., McKinney, S., Wang, Y., Yu, Z., Park, J., Semerad, C., Ross, E., *et al.* (2018). Prospectively isolated Tetraspanin^{+} neoblasts are adult pluripotent stem cells underlying planaria regeneration. Cell *173*, 1593-1608.e20.

21. Reddien, P.W., Oviedo, N.J., Jennings, J.R., Jenkin, J.C., and Sánchez Alvarado, A. (2005). SMEDWI-2 is a PIWI-like protein that regulates planarian stem cells. Science *310*, 1327–1330.

22. Scimone, M.L., Wurtzel, O., Malecek, K., Fincher, C.T., Oderberg, I.M., Kravarik, K.M., and Reddien, P.W. (2018). *foxF-1* Controls Specification of Non-body Wall Muscle and Phagocytic Cells in Planarians. Curr. Biol. *28*, 3787-3801.e6.

23. Tu, K.C., Cheng, L.-C., T K Vu, H., Lange, J.J., McKinney, S.A., Seidel, C.W., and Sánchez Alvarado, A. (2015). Egr-5 is a post-mitotic regulator of planarian epidermal differentiation. eLife *4*, e10501.

24. Cheng, L.-C., Tu, K.C., Seidel, C.W., Robb, S.M.C., Guo, F., and Sánchez Alvarado, A. (2018). Cellular, ultrastructural and molecular analyses of epidermal cell development in the planarian *Schmidtea mediterranea*. Dev. Biol. *433*, 357–373.

25. Forsthoefel, D.J., James, N.P., Escobar, D.J., Stary, J.M., Vieira, A.P., Waters, F.A., and Newmark, P.A. (2012). An RNAi screen reveals intestinal regulators of branching morphogenesis, differentiation, and stem cell proliferation in planarians. Dev. Cell *23*, 691–704.

26. Hoffman, M., and Wurtzel, O. (2023). PLANAtools-An interactive gene expression repository for the planarian *Schmidtea mediterranea*. Front. Cell Dev. Biol. *11*, 1149537.

27. Fincher, C.T., Wurtzel, O., de Hoog, T., Kravarik, K.M., and Reddien, P.W. (2018). Cell type transcriptome atlas for the planarian *Schmidtea mediterranea*. Science *360*.

28. Currie, K.W., Molinaro, A.M., and Pearson, B.J. (2016). Neuronal sources of hedgehog modulate neurogenesis in the adult planarian brain. eLife *5*.

29. Reddien, P.W., Bermange, A.L., Murfitt, K.J., Jennings, J.R., and Sánchez Alvarado, A. (2005). Identification of genes needed for regeneration, stem cell function, and tissue homeostasis by systematic gene perturbation in planaria. Dev. Cell *8*, 635–649.

bioRxiv preprint doi: https://doi.org/10.1101/2024.02.26.582030; this version posted February 28, 2024. The copyright holder for this preprint (which was not certified by peer review) is the author/funder, who has granted bioRxiv a license to display the preprint in perpetuity. It is made available under aCC-BY-NC-ND 4.0 International license.

30. Wenemoser, D., Lapan, S.W., Wilkinson, A.W., Bell, G.W., and Reddien, P.W. (2012). A molecular wound response program associated with regeneration initiation in planarians. Genes Dev. *26*, 988–1002.

31. Sandmann, T., Vogg, M.C., Owlarn, S., Boutros, M., and Bartscherer, K. (2011). The head-regeneration transcriptome of the planarian *Schmidtea mediterranea*. Genome Biol. *12*, R76.

32. Pearson, B.J., and Sánchez Alvarado, A. (2010). A planarian p53 homolog regulates proliferation and self-renewal in adult stem cell lineages. Development *137*, 213–221.

33. Zhu, S.J., Hallows, S.E., Currie, K.W., Xu, C., and Pearson, B.J. (2015). A mex3 homolog is required for differentiation during planarian stem cell lineage development. eLife *4*.

34. Scimone, M.L., Meisel, J., and Reddien, P.W. (2010). The Mi-2-like *Smed-CHD4* gene is required for stem cell differentiation in the planarian *Schmidtea mediterranea*. Development *137*, 1231–1241.

35. Dagan, Y., Yesharim, Y., Bonneau, A.R., Frankovits, T., Schwartz, S., Reddien, P.W., and Wurtzel, O. (2022). m6A is required for resolving progenitor identity during planarian stem cell differentiation. EMBO J. *41*, e109895.

36. Li, L., and Xie, T. (2005). Stem cell niche: structure and function. Annu. Rev. Cell Dev. Biol. *21*, 605–631.

37. Morrison, S.J., and Spradling, A.C. (2008). Stem cells and niches: mechanisms that promote stem cell maintenance throughout life. Cell *132*, 598–611.

38. Chan, A., Ma, S., Pearson, B.J., and Chan, D. (2021). Collagen IV differentially regulates planarian stem cell potency and lineage progression. Proc Natl Acad Sci USA *118*.

39. Ferraro, F., Celso, C.L., and Scadden, D. (2010). Adult stem cels and their niches. Adv. Exp. Med. Biol. *695*, 155–168.

40. Baguñà, J. (2012). The planarian neoblast: the rambling history of its origin and some current black boxes. Int. J. Dev. Biol. *56*, 19–37.

41. Adler, C.E., and Sánchez Alvarado, A. (2015). Types or states? cellular dynamics and regenerative potential. Trends Cell Biol. *25*, 687–696.

42. Salvetti, A., Rossi, L., Bonuccelli, L., Lena, A., Pugliesi, C., Rainaldi, G., Evangelista, M., and Gremigni, V. (2009). Adult stem cell plasticity: neoblast repopulation in non-lethally irradiated planarians. Dev. Biol. *328*, 305–314.

43. Wang, I.E., Wagner, D.E., and Reddien, P.W. (2018). Clonal Analysis of Planarian Stem Cells by Subtotal Irradiation and Single-Cell Transplantation. Methods Mol. Biol. *1774*, 479–495.

44. Steele, V.E., and Lange, C.S. (1976). Effects of irradiation on stem cell response to differentiation inhibitors in the planarian *Dugesia etrusca*. Radiat. Res. *67*, 21–29.

bioRxiv preprint doi: https://doi.org/10.1101/2024.02.26.582030; this version posted February 28, 2024. The copyright holder for this preprint (which was not certified by peer review) is the author/funder, who has granted bioRxiv a license to display the preprint in perpetuity. It is made available under aCC-BY-NC-ND 4.0 International license.

765 45. Hayashi, T., Asami, M., Higuchi, S., Shibata, N., and Agata, K. (2006). Isolation of planarian X-ray-
766 sensitive stem cells by fluorescence-activated cell sorting. Dev. Growth Differ. *48*, 371–380.

767 46. LoCascio, S.A., Lapan, S.W., and Reddien, P.W. (2017). Eye Absence Does Not Regulate Planarian
768 Stem Cells during Eye Regeneration. Dev. Cell *40*, 381-391.e3.

769 47. Petersen, C.P., and Reddien, P.W. (2008). Smed-betacatenin-1 is required for anteroposterior
770 blastema polarity in planarian regeneration. Science *319*, 327–330.

771 48. Gaviño, M.A., and Reddien, P.W. (2011). A Bmp/Admp regulatory circuit controls maintenance
772 and regeneration of dorsal-ventral polarity in planarians. Curr. Biol. *21*, 294–299.

773 49. Wurtzel, O., Oderberg, I.M., and Reddien, P.W. (2017). Planarian Epidermal Stem Cells Respond
774 to Positional Cues to Promote Cell-Type Diversity. Dev. Cell *40*, 491-504.e5.

775 50. Tasaki, J., Shibata, N., Nishimura, O., Itomi, K., Tabata, Y., Son, F., Suzuki, N., Araki, R., Abe, M.,
776 Agata, K., *et al.* (2011). ERK signaling controls blastema cell differentiation during planarian
777 regeneration. Development *138*, 2417–2427.

778 51. Fan, Y., Chai, C., Li, P., Zou, X., Ferrell, J.E., and Wang, B. (2023). Ultrafast distant wound response
779 is essential for whole-body regeneration. Cell *186*, 3606-3618.e16.

780 52. Wurtzel, O., Cote, L.E., Poirier, A., Satija, R., Regev, A., and Reddien, P.W. (2015). A Generic and
781 Cell-Type-Specific Wound Response Precedes Regeneration in Planarians. Dev. Cell *35*, 632–645.

782 53. Rouhana, L., Weiss, J.A., Forsthoefel, D.J., Lee, H., King, R.S., Inoue, T., Shibata, N., Agata, K., and
783 Newmark, P.A. (2013). RNA interference by feeding in vitro-synthesized double-stranded RNA to
784 planarians: methodology and dynamics. Dev. Dyn. *242*, 718–730.

785 54. King, R.S., and Newmark, P.A. (2013). In situ hybridization protocol for enhanced detection of
786 gene expression in the planarian *Schmidtea mediterranea*. BMC Dev. Biol. *13*, 8.

787 55. King, R.S., and Newmark, P.A. (2018). Whole-Mount In Situ Hybridization of Planarians. Methods
788 Mol. Biol. *1774*, 379–392.

789 56. Choi, H.M.T., Schwarzkopf, M., Fornace, M.E., Acharya, A., Artavanis, G., Stegmaier, J., Cunha, A.,
790 and Pierce, N.A. (2018). Third-generation in situ hybridization chain reaction: multiplexed,
791 quantitative, sensitive, versatile, robust. Development *145*.

792 57. Wenemoser, D., and Reddien, P.W. (2010). Planarian regeneration involves distinct stem cell
793 responses to wounds and tissue absence. Dev. Biol. *344*, 979–991.

794 58. Rueden, C.T., Schindelin, J., Hiner, M.C., DeZonia, B.E., Walter, A.E., Arena, E.T., and Eliceiri, K.W.
795 (2017). ImageJ2: ImageJ for the next generation of scientific image data. BMC Bioinformatics *18*,
796 529.

797 59. Pellettieri, J. (2010). Cell death and tissue remodeling in planarian regeneration. Dev Biol.

798 60. Drevon, D., Fursa, S.R., and Malcolm, A.L. (2017). Intercoder reliability and validity of
799 webplotdigitizer in extracting graphed data. Behav. Modif. *41*, 323–339.